SP Science Press

ARTICLE

Temperature Field Simulation and Experiment of Sliding-Pressure Additive Manufacturing Based on Joule Heat

Li Suli[1,2,3],   Xiong Jie[1],   Gao Zhuang[1],   Ma Kaiyue[1],   Lv Jiawen[2],   Gao Yang[1],   Yang Laixia[1], Lu Bingheng[2,3]

[1] College of Mechanical Engineering, Xi'an University of Science and Technology, Xi'an 710054, China; [2] National Innovation Institute of Additive Manufacturing, Xi'an 710300, China; [3] State Key Laboratory for Manufacturing System Engineering, Xi'an Jiaotong University, Xi'an 710049, China

Abstract: A sliding-pressure additive manufacturing technique with low cost and high accuracy based on Joule heat (SP-JHAM) was developed for the small metal parts. The temperature field and thermal history of the system are important for the experiment analysis. In this research, a thermal-electrical-structural coupling finite element simulation model for three-dimensional SP-JHAM process was established. The temperature field variation law during manufacturing, the temperature distributions inside the wire and substrate, and the shape of isothermal surfaces were analyzed. Results show that the Joule heat is generated between the wire and roller, and the internal temperature of wire rises to 2700 °C within 0.1 s. The position of the maximum temperature is moved with the roller moving. The temperature gradient inside the wire presents the arching shape, and that inside the substrate presents the semi-ellipsoidal shape. The simulated cross-section melting regions are in good agreement with the experimental ones. Thus, the established finite element model can accurately simulate the temperature field of SP-JHAM process, which is of great significance for the guidance of mechanism investigation and actual production.

Key words: additive manufacturing; Joule heat; thermal-electric-structural coupling; temperature field simulation

Additive manufacturing (AM) is an advanced manufacturing technique, which has been rapidly developed in the past 30 years. Due to its low cost, short duration, and high personalized degree, AM has been widely used in various manufacturing industries[1–2]. The raw materials used for AM are usually metal and non-metal materials[3]. Currently, the forming methods for metal processing mainly include selective laser sintering[4–5], selective laser melting[6–7], direct metal laser sintering[8–9], electron beam selective melting[10–11], and wire arc additive manufacturing[12–13]. The principle of AM technique is to directly heat the metal through a high-energy beam, which requires complex equipment and high power input. In order to simplify the operation, improve energy efficient, and reduce manufacturing cost, the sliding-pressure additive manufacturing based on Joule heat (SP-JHAM)

process was proposed. Joule heat can be used to heat the wire, and it can be generated in the contact area and inside the wire, which is more favorable for energy utilization and cost control.

Chen et al[14] used current to produce Joule heat by shorted wire and substrate to melt the wire. The heat generation mechanism and melting behavior of wire melt drop transition have been investigated, and the results show that the variation trends of dynamic resistance to melt the wire are the same under the direct current and pulse current conditions. Thus, the plastic deformation of the wire with different currents is also studied, revealing the deformation law of wire under different conditions. The resistance additive manufacturing[15] and SP-JHAM[16] have also been thoroughly researched. During these manufacturing processes, the temperature

changes rapidly within a short period, and the temperature variation history is closely related to the final quality of forming parts.

However, it is difficult to accurately obtain the detailed temperature fields and thermal history during experiments. In recent years, numerical simulation has become a critical method to study the temperature field in metal AM processes[17–20]. Currently, in the simulation of metal AM processes, the primary heat source is usually an external heat source. The common method for heat source simulation is to apply a surface heat source, a body heat source, or a mixed heat source to the model. Theoretically, the simulation accuracy of SP-JHAM process with external heat source is worse than that with other heat sources, such as laser and arc, because Joule heat is produced by the electrical resistance within the metal and by the contact resistance between the metals. The numerical simulation on the temperature field of SP-JHAM process is rarely conducted.

Therefore, in this research, a thermal-electric-structural coupling finite element model was established to simulate the temperature field and thermal history of SP-JHAM process. The accuracy of finite element model was verified through experiments. This research provided guidance for the finite element simulation method of SP-JHAM process.

1 Experiment

The schematic diagram of SP-JHAM process is shown in
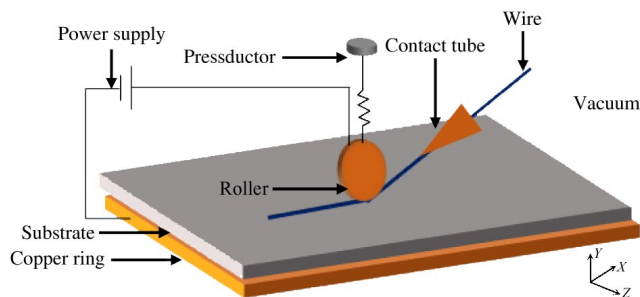
Fig.1   Schematic diagram of SP-JHAM process

Fig. 1. The positive electrode of the power supply was connected to the roller, and the negative electrode was connected to the copper ring below the substrate. A downward motion was applied onto the roller to pre-press and hold the metal wire until the printing was completed. A pressure sensor recorded the pressure value to ensure the well connection among the roller, wire, substrate, and copper ring to obtain the smooth current flow. After pre-loading, a programmable power supply was used to apply a current to the system, therefore forming a closed loop and generating Joule heat to metallurgically bond the wire and substrate. When the current reached the maximum state, the substrate and the copper ring moved along the *X*-axis direction. The subsequent wire was also metallurgically bonded to the substrate by Joule heat. When the motion stopped, the power supply stopped, the roller was lifted, and a single layer was obtained by SP-JHAM process.

The equipment of SP-JHAM experiment system is shown in Fig. 2. The programmable power supply was IT-M3910D-10-1020 (ITECH, Nanjing, China). The motion of the substrate-copper ring and the direction of the roller were controlled through the numerical control machine of type M1 by computer. The three-axis linkage control could be realized by the open-source numerical control system of Windows. The environment was set as a vacuum chamber, and the vacuum environment was achieved by vacuum pumps. FA402B pressure sensor (FIBOS Company) was used with range of 20 N, and FA13 amplifier was used to calibrate and measure the pressure values.

The 304 stainless steel wire with cross section of 0.2 mm× 0.2 mm was used as the feedstock because it has excellent corrosion resistance, high strength, and high plasticity, which is widely used in the power industry, steam turbine manufacturing industry, and medicine[21]. The 316L stainless steel plate with dimension of 100 mm×100 mm×3 mm was used as the substrate material. The chemical composition of 304 and 316L stainless steels is shown in Table 1. The material of the roller and copper ring was CuCrZr, and the thermal physical properties of stainless steels and CuCrZr are listed in Table 2.

Fig.2   Equipment set of SP-JHAM process

Table 1   Chemical composition of 316L and 304 stainless steels (wt%)[16]

Material	Cr	Mn	Mo	Ni	Si	C	P	S	Fe
316L	16.38	0.86	2.11	10.11	0.44	0.018	0.026	0.007	68.33
304	18.01	0.77	0.03	8.03	0.47	0.052	0.027	0.003	69.34

2 Finite Element Model

2.1 Geometric model and meshing

To simplify the calculations and to apply the boundary conditions, a finite element model of SP-JHAM process was simply established. The substrate size was reduced to 10 mm× 10 mm×3 mm, and the corresponding copper ring size was also reduced to 10 mm×10 mm×1 mm. Meanwhile, the wall thickness of the copper ring was 1 mm. The upper half of the roller was cut away for convenient loading of model. The dimension of the metal wire in the model was 0.2 mm× 0.2 mm×8 mm. After the assembly was completed, the roller was placed directly above the metal wire, and the roller bottom was tangent to the upper surface of the metal wire. The model was divided into the grids with overall mesh size of 0.2 mm.

The mesh of the temperature concentration region was subdivided with the minimum mesh size of 0.01 mm. The schematic diagrams of finite element model are shown in Fig.3.

2.2 Thermal-electrical-structural coupling

The SP-JHAM process is a complex process involving the multiple physical fields and multiple scales. During the process, the motion of the substrate-copper ring and the pre-loading of wire by roller should be investigated by transient structural analysis. The energization process should be investigated by transient electrical analysis. The generation of Joule heat after electrification as well as the heat conduction between different parts should be investigated by transient thermal analysis. Based on these information, a transient fully-coupled thermal-electrical-structural model was used to simulate the SP-JHAM process in this research. A fully-coupled thermal-electrical-structural analysis consisted of a coupled thermal-displacement analysis and a coupled thermal-electrical analysis.

2.2.1 Coupled thermal-electrical analysis

The heat generation in SP-JHAM process is attributed

Table 2   Thermal physical properties of stainless steel and CuCrZr materials[22]

Temperature/°C	Stainless steel			Copper electrode (CuCrZr)		
	Specific heat/ $J \cdot kg^{-1} \cdot °C^{-1}$	Heat conductivity/ $W \cdot m^{-1} \cdot °C^{-1}$	Specific resistance/ $\times 10^{-8} \ \Omega \cdot m$	Specific heat/ $J \cdot kg^{-1} \cdot °C^{-1}$	Heat conductivity/ $W \cdot m^{-1} \cdot °C^{-1}$	Specific resistance/ $\times 10^{-8} \ \Omega \cdot m$
21	412	20.0	72	397.8	390.0	2.64
93	445	20.1	77	401.9	380.6	3.00
204	502	20.2	85	418.7	370.0	4.00
316	551	20.4	93	431.2	355.0	5.05
427	622	20.6	101	439.6	345.4	5.63
538	858	20.7	107	452.2	334.7	6.06
649	876	21.0	113	464.7	320.0	8.31
760	889	21.5	119	471.5	315.5	19.14
871	657	22.0	124	477.3	310.3	22.03
982	643	21.0	135	485.4	305.0	26.03
1093	690	20.0	150	497.8	300.1	31.69
1200	711	19.7	164	502.4	-	34.87
1500	1082	38.19	197	-	-	38.24
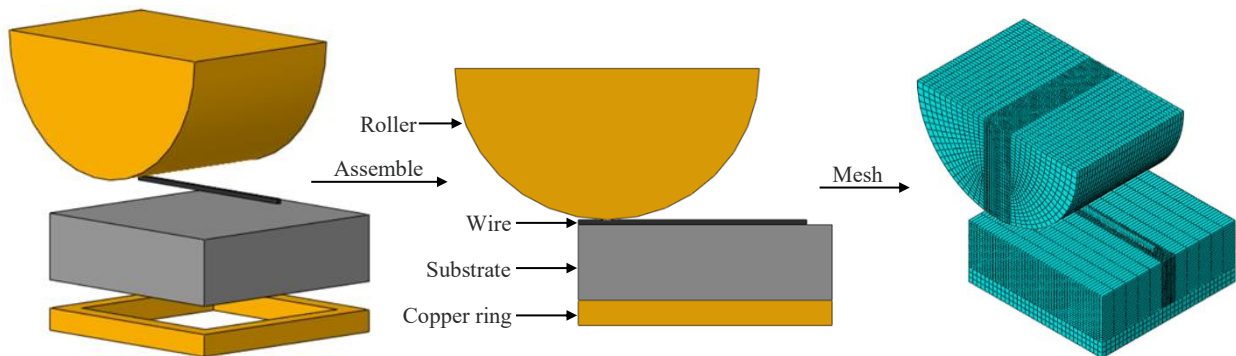
Fig.3   Schematic diagrams of finite element model of SP-JHAM process

to the Joule heat. Joule heat is governed by the Joule's law, and it describes the power dissipation rate P_{ec} of electric current flowing (J) through a conductor, as expressed by Eq.(1):

$$\begin{cases} \boldsymbol{J} = \sigma^E \cdot \boldsymbol{E} \\ \boldsymbol{E} = -\dfrac{\partial \varphi}{\partial x} \\ P_{ec} = \boldsymbol{E} \cdot \boldsymbol{J} = \dfrac{\partial \varphi}{\partial x} \cdot \sigma^E \cdot \dfrac{\partial \varphi}{\partial x} \end{cases} \tag{1}$$

where $\sigma^E(\theta, f^\alpha)$ is the electrical conductivity matrix; θ is the temperature; f^α with $\alpha = 1, 2\cdots$ are any predefined field variables; $\boldsymbol{E}$ is the electrical field intensity; φ is the potential at a certain point inside the electric field; x is the distance from the zero potential surface. The amount of released energy is considered as internal heat $\eta_v P_{ec}$, where η_v is an energy conversion factor.

The heat $\boldsymbol{Q}$ can be calculated by Joule's law, which is governed by Eq.(2), as follows:

$$\boldsymbol{Q} = \int_0^t i^2(\boldsymbol{t}) \boldsymbol{R}(\boldsymbol{t}) \mathrm{d}\boldsymbol{t} \tag{2}$$

where $i(\boldsymbol{t})$ is the current value in the system; $\boldsymbol{R}(\boldsymbol{t})$ is the total resistance value in the system; $\boldsymbol{t}$ is the power-on time.

The SP-JHAM process should be investigated by transient thermal analysis. The fundamental equation of non-steady-state heat conduction obeys the Fourier's law, as follows:

$$\rho c \frac{\partial T}{\partial t} = \frac{\partial}{\partial x}\left(\lambda \frac{\partial T}{\partial x}\right) + \frac{\partial}{\partial y}\left(\lambda \frac{\partial T}{\partial y}\right) + \frac{\partial}{\partial z}\left(\lambda \frac{\partial T}{\partial z}\right) + \boldsymbol{Q} \tag{3}$$

where T is the temperature function related to coordinates x, y, and z as well as time t; c is the specific heat capacity of the material; ρ is the material density; λ is the thermal conductivity of the material; $\boldsymbol{Q}$ is the generated heat per unit volume.

The thermal balance formula is expressed by Eq. (4), as follows:

$$W = W_1 + W_2 + W_3 \tag{4}$$

where W is the total heat; W_1 is the heat required for metallurgical bonding between the metal wire and the substrate; W_2 is the heat conduction; W_3 is the heat loss due to convection and radiation. In this research, since the process was conducted under the vacuum environment, only the radiation heat loss was considered, as expressed by Eq.(5):

$$q = \sigma\epsilon\left[\left(\theta - \theta^Z\right)^4 - \left(\theta_0 - \theta^Z\right)^4\right] \tag{5}$$

where q is the heat flux per unit area; θ is the surface temperature of parts; θ_0 is the ambient temperature; θ^Z is the absolute zero temperature; ϵ is the surface emissivity; σ is the Boltzmann constant.

2.2.2   Coupled thermal-displacement analysis

The thermal-displacement coupling is mainly reflected by the thermal expansion of the material during the metal heating and the significant change in the thermal physical properties of the materials due to the rapid temperature evolution. In this research, the part movement and the change of Joule heat generation region during the printing process can also reflect the thermal-displacement coupling.

The Von Mises yield criterion was used. The plastic behavior of the material satisfies the plastic theory. The stress and strain satisfy the instantaneous linear relationship. According to the incremental theory, the governing equation for stress and strain increments is expressed by Eq. (6), as follows:

$$\mathrm{d}\sigma = \boldsymbol{D}_{ep}\mathrm{d}\varepsilon \tag{6}$$

where $\mathrm{d}\sigma$ is the stress increment; $\boldsymbol{D}_{ep}$ is the elastic-plastic stress-strain matrix; $\mathrm{d}\varepsilon$ is the total strain increment.

The elastic-plastic stress-strain matrix can be obtained by simple calculation of the elastic and plastic matrices, as follows:

$$\boldsymbol{D}_{ep} = \boldsymbol{D}_e - \boldsymbol{D}_p \tag{7}$$

where $\boldsymbol{D}_e$ is the elastic stress-strain matrix; $\boldsymbol{D}_p$ is the plastic stress-strain matrix.

The total strain increment $\mathrm{d}\varepsilon$ consists of three parts: elastic strain increment $\mathrm{d}\varepsilon_e$, plastic strain increment $\mathrm{d}\varepsilon_p$, and thermal strain increment $\mathrm{d}\varepsilon_T$. Thus, the governing equation can be expressed by Eq.(8), as follows:

$$\mathrm{d}\varepsilon = \mathrm{d}\varepsilon_e + \mathrm{d}\varepsilon_p + \mathrm{d}\varepsilon_T \tag{8}$$

The governing equation of thermal strain increment $\mathrm{d}\varepsilon_T$ is shown in Eq.(9), as follows:

$$\mathrm{d}\varepsilon_T = \varepsilon\mathrm{d}T \tag{9}$$

where ε is the thermal expansion coefficient of the material.

The Newton method can be used to realize the asymmetric Jacobian matrix. The strong coupling governing equation of the incremental displacement and temperature is expressed by Eq.(10), as follows:

$$\begin{pmatrix} \boldsymbol{K}_{uu} & \boldsymbol{K}_{u\theta} \\ \boldsymbol{K}_{\theta u} & \boldsymbol{K}_{\theta\theta} \end{pmatrix} \begin{pmatrix} \Delta u \\ \Delta \theta \end{pmatrix} = \begin{pmatrix} \boldsymbol{R}_u \\ \boldsymbol{R}_\theta \end{pmatrix} \tag{10}$$

where Δu and $\Delta\theta$ are the corrections to the incremental displacement and temperature, respectively; $\boldsymbol{K}_{ij}$ is a submatrix of the fully coupled Jacobian matrix; $\boldsymbol{R}_u$ and $\boldsymbol{R}_\theta$ are the mechanical and thermal residual vectors, respectively.

2.3 Load and boundary conditions

Due to the complexity of SP-JHAM process, a multi-analysis step was proposed for the simulation. To improve the convergence of the model calculations, the motion of substrate-copper ring was converted to the motion of roller. Therefore, the analysis was divided into seven steps, including the force loading step, force holding step, current loading step, roller moving step, current unloading step, cooling step, and force unloading step. Fig. 4 shows the timeline of these analysis steps.

In different analysis steps, the system is subjected to different boundary conditions and loads. In the initial analysis step, the surface of each component was set with its corresponding surface emissivity, and the absolute zero temperature (-273.15 °C) and ambient temperature (20 °C) were defined. The specific boundary conditions and loads were described as follows.

(1) All degrees of freedom for transition/rotation of the entire roller, except for the pressure direction, were constrained to 0.

(2) The bottom of the copper ring was fixed, and this
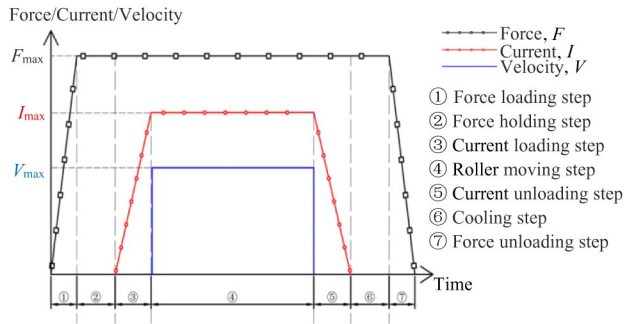
Fig.4   Timeline of analysis steps

surface was defined as a zero potential plane.

(3) In the roller moving step, the degree of freedom for the transition of the roller motion direction was constrained to L with $L=vt$, where v is the speed process parameter and t is the duration of the roller moving step.

(4) During the force loading step, a linearly increasing force was applied to the roller upper surface and held until the force unloading step started.

(5) During the current loading step, a linearly increasing current was applied to the roller upper surface and held until current unloading step started.

2.4 Contact setting and contact resistance

One of the major challenges in the numerical simulation of SP-JHAM process is the interface treatment, especially the contact part between the roller and the wire. Since the contact pair needs to transmit the force, electricity, and temperature parameters during the roller moving step, the conduction coefficients of force, electricity, and temperature between the contact pairs should be set. In this case, the electrical conduction requires the electrical conductivity between two interfaces, which involves the contact resistance. The total resistance value $R(t)$ in the system is composed of four parts: the body resistance of the roller and copper ring (R_e), the body resistance of the wire and substrate (R_w), the contact resistance between the roller and the wire (R_{ew}), and the contact resistance between the wire and the substrate (R_c). Therefore, $R(t) = 2R_e + 2R_w + 2R_{ew} + R_c$, and the schematic diagram of the components of total resistance is shown in Fig.5.

The study of contact resistance can be traced back to the
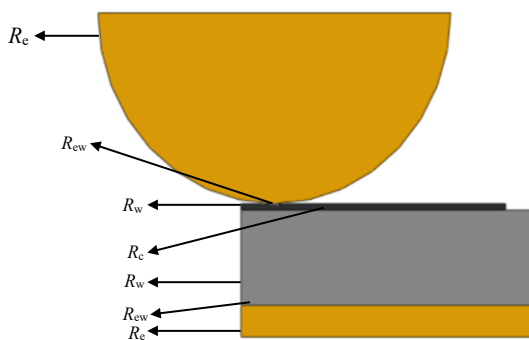
Fig.5   Schematic diagram of components of total resistance

one-dimensional contact resistance finite element model, where the contact resistance is a function of temperature. Currently, the contact resistance is usually considered as a function of contact pressure[23], material hardness[24], and the combined effects of contact pressure and temperature[25]. The thermal and electrical conduction parameters of the contacts in this research are shown in Table 4 and Table 5.

2.5 Experiment parameters

According to the analysis steps in Fig. 4, the specific experiment process parameters were F_{max}=0.8 N, I_{max}=260 A, and V_{max}=200 mm/min. The particular time parameters for seven analysis steps were 0.1, 0.5, 0.1, 6.0, 0.01, 0.5, and 0.1 s. To improve the computational efficiency of the model, the time for the fourth analysis step was set as 0.6 s.

3 Results and Discussion

3.1 Transient temperature field analysis

The primary goal of the 1st and 2nd analysis steps is to establish a complete contact for the entire system, ensuring the current flow in subsequent analyses.

In the third analysis step, the model is sliced along the X-axis in the direction of roller motion to analyze the changes in the 3D temperature field of the system. To provide more intuitive observation of the temperature field of the wire, the roller is set at the semi-transparent state. As shown in Fig.6, it can be observed that with increasing the current to I_{max} value, Joule heat occurs between the wire and roller. The internal temperature of wire rises to 2700 ° C within 0.1 s. With increasing the current, the maximum temperature is also increased. After reaching the maximum current, the temperature field of the system exhibits a symmetrical distribution: the highest temperature occurs at the wire center which is directly below the roller.

During the fourth analysis step, the roller slides along the positive direction of X-axis, which leads to the change in the contact area between the roller and the wire. As a result, the region of Joule heat generation also changes. Path 1 is established by taking equidistant nodes along the middle layer of wire in the motion direction, as shown in Fig.7a. Along the Path 1, the temperature at 0.05, 0.10, 0.15, 0.20, 0.25, 0.30, 0.35, 0.40, 0.45, 0.50, 0.55, and 0.60 s during the fourth analysis step is recorded, as shown in Fig.7b. The temperature field of Path 1 is changed with varying the time and position, as shown in Fig. 7b. It can be observed that during this

Table 4   Contact coefficients between wire and substrate[26]

Temperature/°C	Thermal conductance/ mW·mm^{-2}·K^{-1}	Electrical conductance/ mΩ^{-1}·mm^{-2}
20	140	6.4
205	150	6.4
425	-	6.5
650	160	6.7
870	160	8.5
1093	-	14.3

Table 5 Contact coefficients between roller/wire and substrate/ copper ring[26]

Temperature/°C	Thermal conductance/ mW·mm^{-2}·K^{-1}	Electrical conductance/ mΩ^{-1}·mm^{-2}
20	560	12.7
205	640	14.9
425	-	20.4
650	1300	53.2
870	4800	-
1093	-	-

analysis step, at t=0 s, the highest temperature is located at X=0 mm. With the step proceeding, the roller is moved, the region of Joule heat generation is changed. However, the entire temperature field does not simply move with the roller. The highest temperature in the temperature field changes continuously, although the change amplitude is small. This is because the heat conduction and radiation heat dissipation reach the thermal equilibrium with Joule heat. The specific temperature changes are shown in Fig.7c.

During the fifth analysis step, the input current decreases from I_{max} to 0 within 0.01 s. However, the temperature field of the system does not reduce significantly during this step, and the highest temperature only decreases by $10-20$ °C. Additionally, in the sixth analysis step, the system temperature rapidly decreases: within the initial 0.1 s, the highest temperature decreases by nearly 2500 °C; in the next 0.4 s, the temperature decreases from 180 °C to 77 °C. In conclusion,

after pre-loading, the Joule heat is generated between the roller and the wire with increasing the current. In the roller moving step, the region of Joule heat generation moves along with the roller. After the roller stops moving and the current is unloaded, the system temperature drops to about 70 °C within 0.5 s. After cooling, the highest temperature region is located in the front half of the wire due to its larger thermal accumulation, compared with that of the back part. The temperature decreases more slowly when it gets closer to the position directly below the roller. The temperature field variations of cooling process (the sixth analysis step) are shown in Fig.8.

3.2 Specific temperature field analysis

The temperature field at t=0.3 s during the fourth analysis step is shown in Fig. 9a. Path 2 was established by taking equidistant nodes along the wire in the Y-axis direction. The temperatures of all nodes along Path 2 were recorded and analyzed, and the results are shown in Fig.9b.

As shown in Fig. 9a, it is obvious that the temperature distribution of the wire along Y-axis direction exhibits the increasing trend firstly and then the decreasing trend. This is because after the generation of Joule heat at the contact surface, the intrinsic resistance of wire becomes a major part of the overall electrical resistance. Therefore, the temperature of contact region between the wire surface and the roller is relatively lower than that inside the wire. According to Fig.9b, it is clear that the width of the area with temperature above the melting point exceeds the wire thickness, indicating that the temperature of some parts of the substrate surface is higher than the melting point. This phenomenon provides favorable temperature conditions for
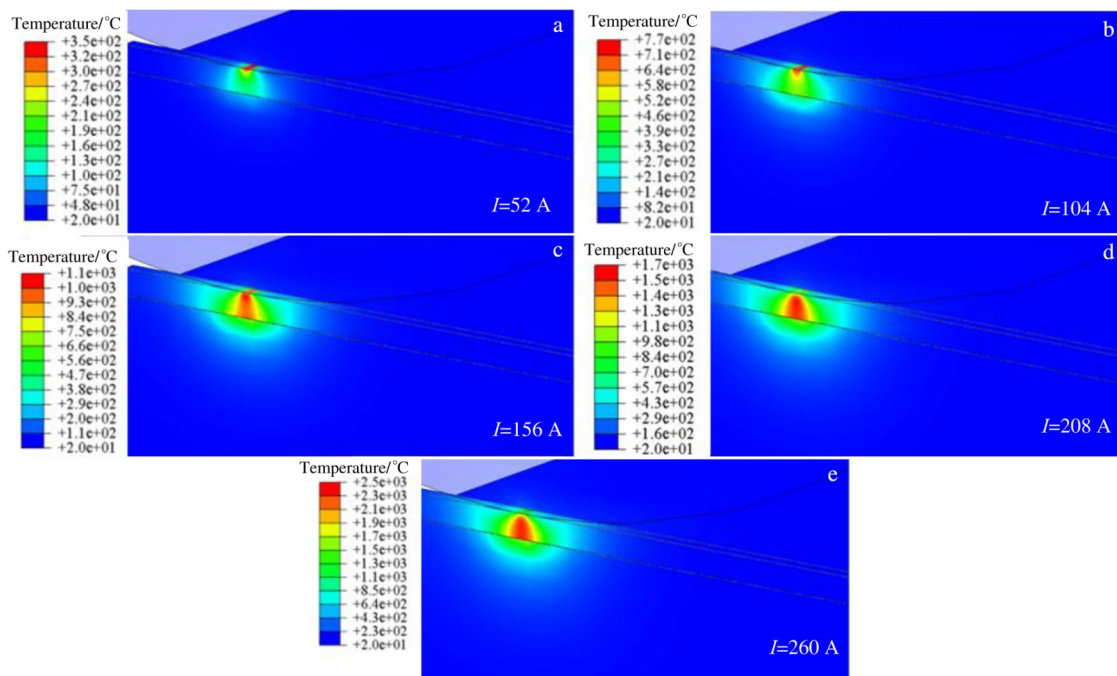
Fig.6 Temperature field variations in the third analysis step: (a) t=0.02 s; (b) t=0.04 s; (c) t=0.06 s; (d) t=0.08 s; (e) t=0.10 s
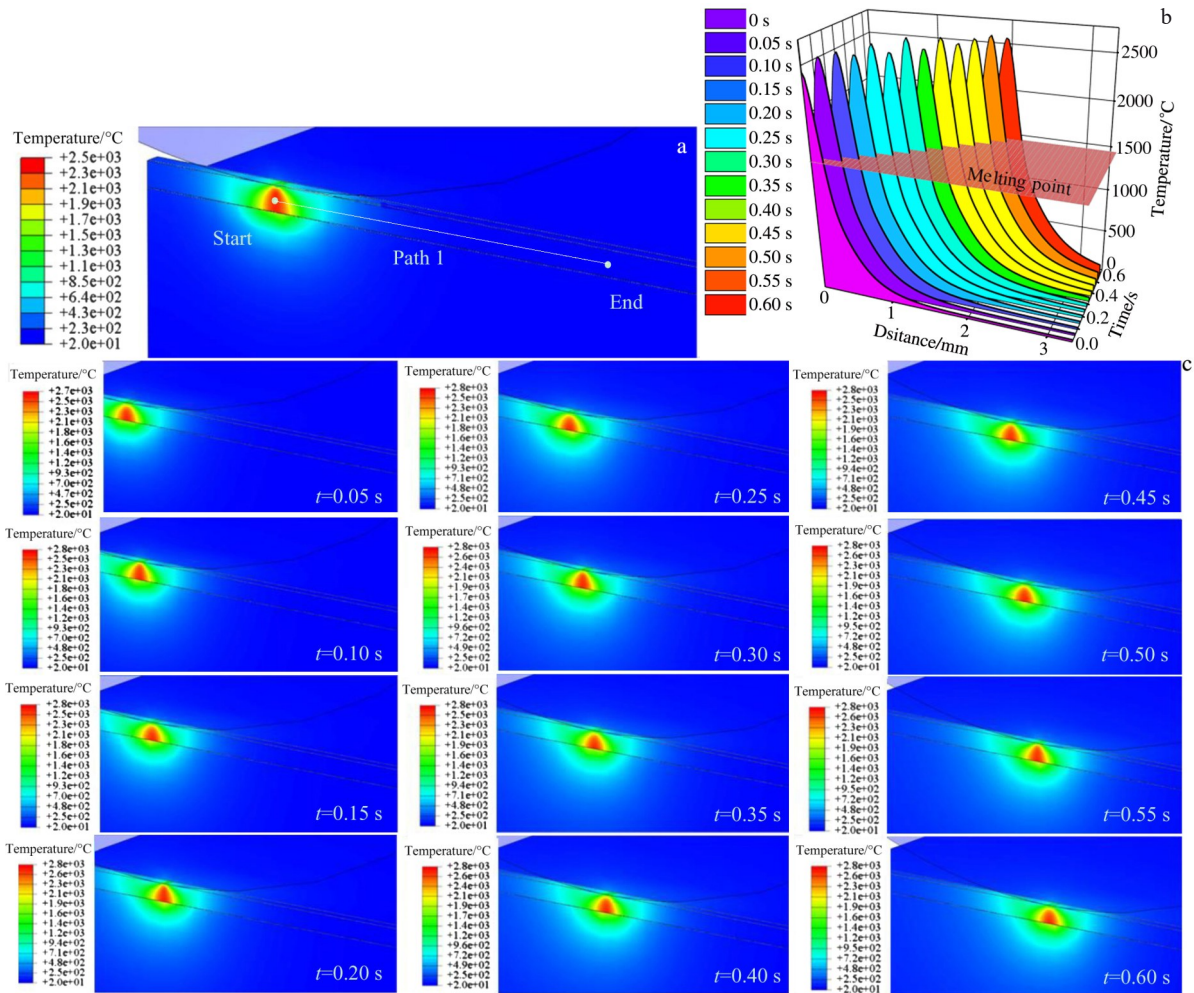
Fig.7   Schematic diagram of temperature field along Path 1 (a); temperature variations in the fourth analysis step (b); temperature fields at different times in the fourth analysis step (c)

the metallurgical bonding between the metal wire and the substrate. As a result, the area with the temperature above metal melting point includes some areas of wire and substrate. After the roller moves, the high-temperature region undergoes cooling and crystallization processes, completing the printing process.

The isothermal surfaces of the wire and substrate are shown in Fig. 10. It can be observed that the isothermal surfaces inside the wire exhibit an arch-bridge-like shape. With increasing the distance between the roller and the position directly below the roller, the span and height of the arch surface are gradually increased, and the vertical temperature gradient is more compact than the horizontal one. Besides, the temperature gradient along the direction of wire motion is more compact than that along the opposite direction. However, the isothermal surface of the substrate presents a semi-ellipsoid shape. The closer the semi-ellipsoid isothermal surface to the lower right side the roller, the shorter the axis, and the denser the isothermal surface. The isothermal surface along the roller motion direction is more compact than that along the opposite direction, which

presents the same characteristics as those of the isothermal surface inside the wire. Different isothermal surfaces are generated inside the wire and the substrate. This is because the contact area between the roller and wire is smaller than that between the wire and substrate. As a result, with increasing the distance between the roller and the position below the roller center, the height and span of the arch shape and the semi-axis length of the semi-ellipsoidal shape are increased.

3.3 Experiment and simulation

To verify the reliability of SP-JHAM finite element model based on the thermal-electric-structural coupling method, experiments were conducted with 304 stainless steel wire. The as-printed parts were cut, sampled, ground, and polished along the direction perpendicular to the heating direction. The simulated and experimental cross section morphologies of experiment object are shown in Fig. 11a, and the appearance and sampling position of the experiment object are shown in Fig. 11b. It can be seen that the cross-sectional melting regions of the simulated object are in good agreement with the experimental ones. Therefore, the finite element model
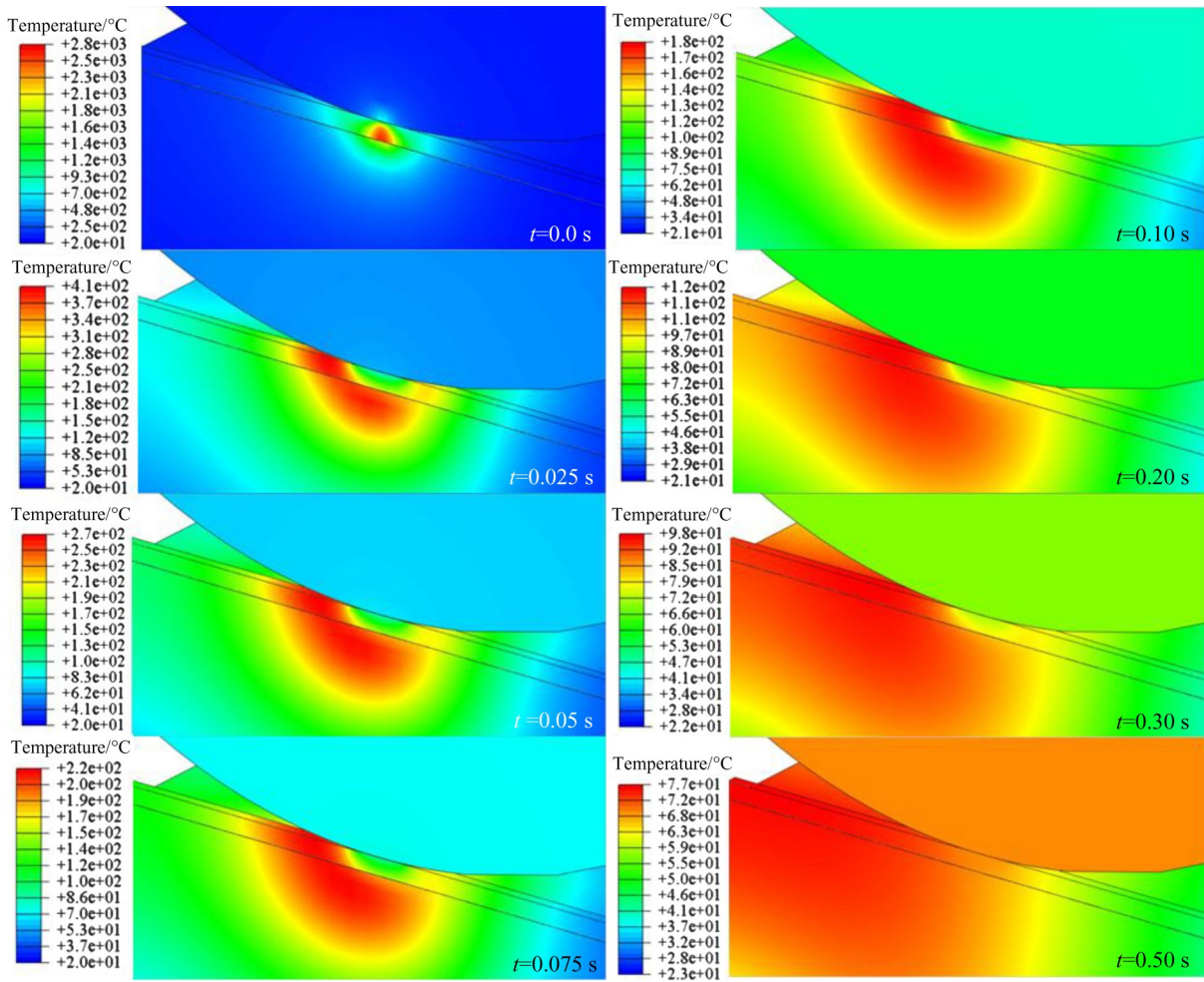
Fig.8   Temperature field variations during the sixth analysis step
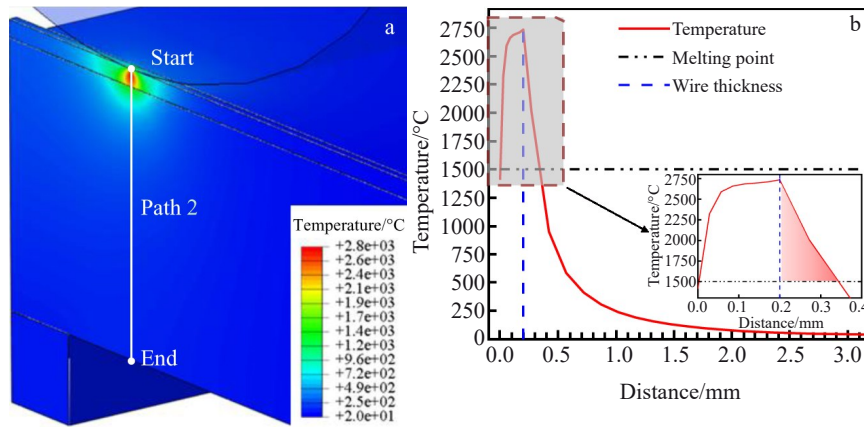
Fig.9   Schematic diagram of Path 2 (a) and temperature field distribution along Path 2 (b) at *t*=0.3 s of the fourth analysis step

shows good reliability. However, slight differences between the simulated and experimental results still exist. This is due to the lack of sufficiently accurate data of material properties for simulation analysis. Besides, because the fluid flow is neglected, the experimental melting height is slightly lower; because the experimental equipment is simplified in the simulation, the actual heat lost by heat conduction is higher than the simulated one. Thus, the experimental melting depth is slightly shallower than the simulated depth.
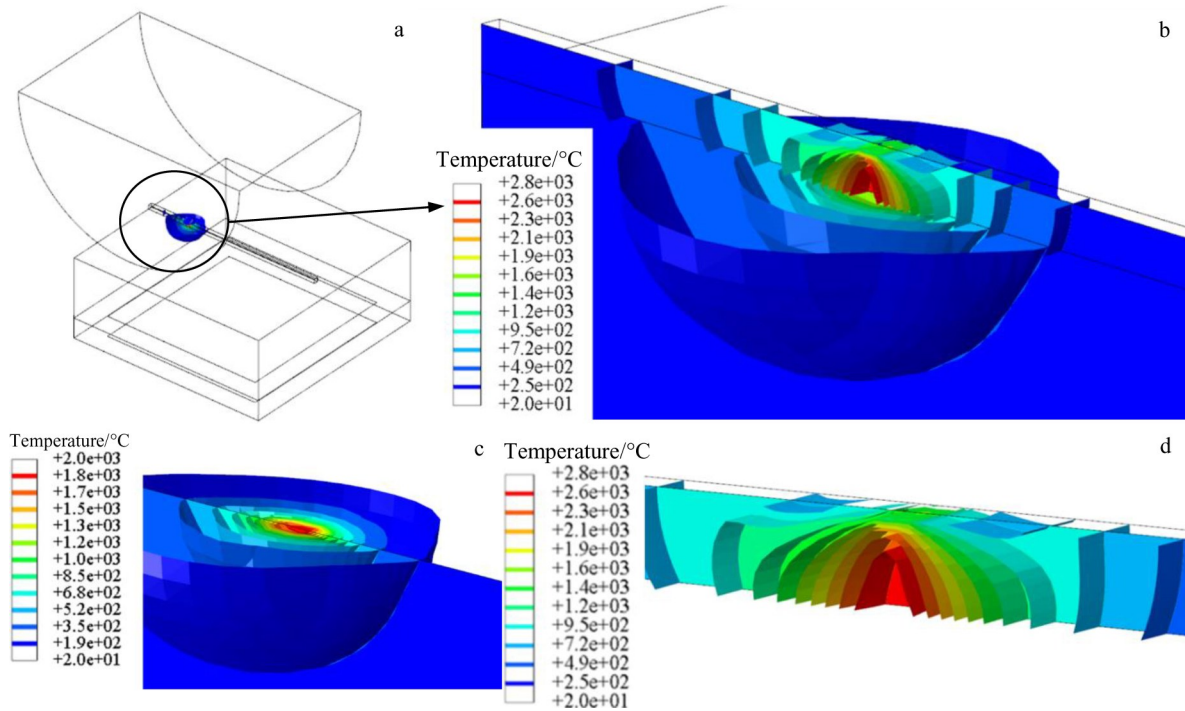
Fig.10   Different isothermal surfaces at *t*=0.3 s: (a) system surface; (b) wire-substrate surface; (c) substrate surface; (d) wire surface
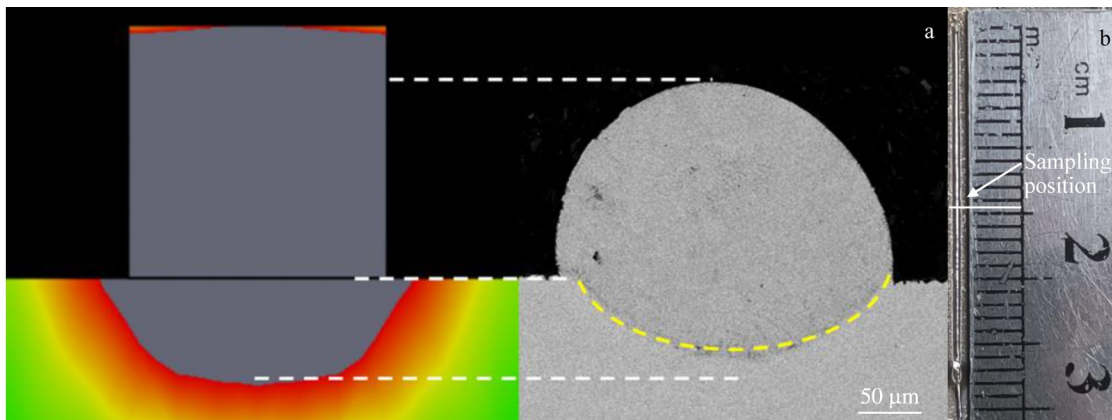
Fig.11   Simulated and experimental cross section morphologies of experiment object (a); appearance and sampling position of experiment object (b)

4 Conclusions

1) The finite element model of the sliding-pressure additive manufacturing technique based on Joule heat shows high accuracy under the premise of ignoring the metal melt flow.

2) After the pre-loading, the Joule heat is generated between the roller and the wire with increasing the current. In the roller moving step, the region of Joule heat generation moves along with the roller. The area with the temperature above metal melting point includes some areas of wire and substrate. After the roller stops moving and the current is unloaded, the system temperature drops to about 70 °C within 0.5 s.

3) When the roller moves, the isothermal surfaces inside the wire form an arch-bridge shape, and the isothermal surfaces of the substrate has the semi-ellipsoidal shape. With increasing

the distance between the roller and the position below the roller center, the height and span of the arch shape and the semi-axis length of the semi-ellipsoidal shape are increased.

References

1   Lu Bingheng. *China Mechanical Engineering*[J], 2020, 31(1): 19 (in Chinese)
2   Schiavone N, Verney V, Askanian H. *3D Printing and Additive Manufacturing*[J], 2020, 7(6): 311
3   Huang Y, Leu M C, Mazumder J *et al*. *Journal of Manufacturing Science and Engineering*[J], 2015, 137(1): 14001
4   Zaharia S M, Pop M A, Buican G R *et al*. *Aerospace*[J], 2023, 10(1): 60

5 Lakraimi R, Abouchadi H, Janan M T *et al. Materials*[J], 2023, 16(2): 753

6 Mao B Y, Liu Y, Ye J W *et al. Rare Metal Materials and Engineering*[J], 2023, 52(3): 860

7 Chen Z, Xiang Y, Wei Z Y *et al. Applied Physics A: Materials Science and Processing*[J], 2018, 124(4): 313

8 Sahu A K, Mahapatra S S. *Machining Science and Technology*[J], 2022, 26(5): 858

9 Km R, Sahoo A K, Routara B C *et al. Proceedings of the Institution of Mechanical Engineers, Part C: Journal of Mechanical Engineering Science*[J], 2023, 237(4): 865

10 Yang Y, Hu L X, Huang J Y. *Materials Characterization*[J], 2023, 196: 112642

11 Li Y, Wang Z W, Shao M H *et al. Vacuum*[J], 2023, 208: 111737

12 Shah I H, Hadjipantelis N, Walter L *et al. Journal of Cleaner Production*[J], 2023, 389: 136071

13 Ju Hongtao, Xu Dongsheng, Shan Feihu *et al. Rare Metal Materials and Engineering*[J], 2020, 49(3): 878 (in Chinese)

14 Chen Shujun, Yuan Chengwei, Jiang Fan *et al. Acta Metallurgical Sinica*[J], 2018, 54(9): 1297 (in Chinese)

15 Li S L, Ma K Y, Xu C *et al. Crystals*[J], 2022, 12(2): 193

16 Ma K Y, Li S L, Xu C *et al. Materials*[J], 2023, 16(5): 2017

17 Li S L, Wei Z Y, Du J *et al Rare Metal Materials and Engineering*[J], 2017, 46(4): 893

18 Wang L, Li H, Wang K H *et al. Applied Physics A: Materials Science and Processing*[J], 2021, 128(5): 447

19 Chen J W, Xiong F Y, Huang C Y *et al. Scinntia Sinica: Physica, Mechanica and Astronomica*[J], 2020, 50(9): 90007

20 Zheng Mingyue, Zhang Shaoming, Hu Qiang *et al. Rare Metal Materials and Engineering*[J], 2019, 48(6): 1819 (in Chinese)

21 Zhang H R, Huang J J, Liu C M *et al. Materials*[J], 2020, 13(16): 3482

22 Vigneshkumar M, Varthanan P A, Raj Y M A. *Transactions of the Indian Institute of Metals*[J], 2019, 72: 429

23 Han Z, Orozco J, Indacochea J E *et al. Welding Research Supplement*[J], 1989, 68(9): 363

24 Dickinson D, Tsai C L, Jammal O. *Journal of Materials and Manufacturing*[J], 1990, 99(5): 789

25 Li Yong Qiang, Zhao He, Zhao Xi Hua *et al. Journal of Jilin University, Engineering and Technology Edition*[J], 2010, 40(3): 709 (in Chinese)

26 Jin Chen. *Numerical Simulation of Welding Process*[M]. Beijing Science and Technology Press, 2017 (in Chinese)

基于焦耳热的滑压式增材制造方法温度场数值模拟与实验

李素丽 [1,2,3]，熊　杰 [1]，高　壮 [1]，马恺悦 [1]，吕佳文 [2]，高　扬 [1]，杨来侠 [1]，卢秉恒 [2,3]

(1. 西安科技大学 机械工程学院，陕西 西安 710054)

(2. 国家增材制造创新中心，陕西 西安 710300)

(3. 西安交通大学 机械制造系统工程国家重点实验室，陕西 西安 710049)

摘　要：提出了一种针对小型金属零部件的低成本、高精度的焦耳热金属熔丝增材制造技术。在此过程中，系统温度场和热历史对于实验分析具有重要意义。本研究主要利用有限元仿真软件建立三维焦耳热金属熔丝增材制造的热-电-结构耦合有限元模型，分析了制造过程中温度场变化规律以及丝材内部和基板的温度分布和等温面形状。结果表明：焦耳热在丝材与滚轮之间产生，丝材内部在0.1 s内升温至2700 ℃，滚轮移动后，最大温度位置随着滚轮的移动而移动，丝材内部温度梯度呈拱形，基板温度梯度呈半椭球形。模拟结果的截面熔核区域与实验截面熔核区域吻合较好。因此，所建立的有限元模型能够较准确地模拟焦耳热熔丝增材制造过程温度场，对实验机理的研究和后期的进一步加工有着重要指导意义。

关键词：增材制造；焦耳热；热-电-结构耦合；温度场模拟

作者简介：李素丽，女，1981 年生，博士，教授，西安科技大学机械工程学院，陕西 西安 710054，E-mail：Lsl15802949318@xust.edu.cn